Low and high frequency variability as a function of spectral properties in the bright X–ray binary GX 5–1

P. G. Jonker[1,2]⋆, M. van der Klis[1], J. Homan[1], M. Méndez[3], W.H.G. Lewin[4],
R. Wijnands[4,5], W. Zhang[6]

[1] *Astronomical Institute "Anton Pannekoek", University of Amsterdam, Kruislaan 403, 1098 SJ Amsterdam*
[2] *Marie Curie Fellow*
[3] *Space Research Organization Netherlands, Sorbonnelaan 2, 3584 CA Utrecht, The Netherlands*
[4] *Department of Physics and Center for Space Research, Massachusetts Institute of Technology, Cambridge, MA 02138*
[5] *Chandra Fellow*
[6] *Laboratory for High Energy Astrophysics, Goddard Space Flight Center, Greenbelt, MD 20771*

1 February 2008

ABSTRACT

We report on a detailed analysis of data obtained over nearly four years with the *Rossi X–ray Timing Explorer* of the Z source GX 5–1. From a spectral analysis using a hardness–intensity diagram it was found that the source traced out the typical Z–shaped pattern. The study of the power spectral properties showed that when the source moved on the Horizontal Branch towards the Normal Branch the fractional rms amplitudes and timescales of all variability decreased, while their FWHMs increased. The frequency separation of the two kHz QPO peaks decreased from 344 ± 12 Hz to 232 ± 13 Hz while the frequency of the lower and upper kHz QPO increased from 172 ± 10 Hz to 608 ± 6 Hz and 516 ± 10 Hz to 840 ± 12 Hz, respectively. At low frequencies, besides the horizontal branch oscillation (HBO) and its second harmonic, two additional broad Lorentzian components were needed to obtain acceptable fits. These broad Lorentzians have Q–values of $\sim$1–2 and have frequencies 0.5 and 1.5 times the HBO frequency. When interpreted as being related to the HBO, they seem to favor disc models for the HBO over the magnetic beat–frequency model. The frequency of the Normal Branch Oscillations changed slightly and non–monotonically while on the Normal Branch between $\sim$6 Hz at both ends and 5.25 ± 0.05 Hz near the middle of the branch. It evolved into a flat–topped noise component on the Flaring Branch. We compared the timing properties of the some of the Z sources. We also compare the timing properties and colour–colour diagrams (CDs) of GX 5–1 with those of the back hole candidate XTE J1550–564 and the atoll source 4U 1608–52. The CDs are strikingly similar when a colour scheme is used that is commonly employed in back hole studies. However, this may be a degeneracy as the CDs turn out to be more complicated when colours common in neutron star studies are employed. Apart from some remarkable similarities between the CD of XTE J1550–564 and that of 4U 1608–52, several differences can be seen between these CDs and that of GX 5–1. Conclusions on spectral states or properties based solely on the use of CDs using the "black hole scheme" should be regarded with caution.

Key words: accretion, accretion discs — stars: individual (GX 5–1) — stars: neutron — X-rays: stars

1 INTRODUCTION

Low–mass X–ray binaries (LMXBs) are systems where the compact object, either a neutron star or a black hole, accretes matter from a companion with a mass of less than 1 $M_\odot$. The neutron–star LMXB systems are subdivided on the

⋆ email : peterj@ast.cam.ac.uk, present address Institute of Astronomy, Cambridge

basis of the pattern they trace out in an X–ray colour–colour or hardness–intensity diagram (CD or HID, respectively) in atoll and Z sources (Hasinger & van der Klis 1989). The X–ray flux measurements combined with the knowledge of the distance have shown that Z sources have a high luminosity ($\sim L_{Edd}$) and accrete at a rate close to the Eddington accretion rate, whereas atoll sources have typical luminosities and inferred accretion rates 5–100 times lower (e.g. see the compilation of source luminosities by Ford et al. 2000). The three branches of the Z traced out in a CD or HID by Z sources are called (from top to bottom); Horizontal Branch, Normal Branch, and Flaring Branch.

Studies of the X–ray variability of Z sources revealed two types of quasi–periodic oscillations (QPOs) with frequencies less than 100 Hz (Horizontal Branch oscillations; HBO and Normal Branch oscillations; NBO), twin kHz QPO peaks, and three types of rapid flickering ("noise"), the very low–frequency noise (VLFN), the low–frequency noise (LFN), and the high–frequency noise (HFN) (see van der Klis 1995; van der Klis 2000 for reviews). The properties of noise features and the HBOs, such as the central frequency and the fractional rms amplitude, are strongly correlated with the position of a source along the Horizontal Branch. These correlations, together with the observed increase in the ultra–violet flux in the Z source Sco X–1 (Vrtilek et al. 1991) when the source moves from the Horizontal Branch via the Normal Branch to the Flaring Branch lend support to the idea that the mass accretion rate increases from the Horizontal Branch via the Normal Branch to the Flaring Branch (see van der Klis 1995). However, recent observations (Wijnands et al. 1996; Di Salvo et al. 2000; Homan et al. 2001a), together with problems noted before (most notably secular motion of the Z track; Kuulkers et al. 1994) show that the situation may be more complex (e.g. van der Klis 2001).

KHz QPOs have now been seen in just over twenty LMXBs, including all Z sources (van der Klis 1998; van der Klis 2000). Potentially they can provide a key to measure the basic properties of neutron stars (spin rates and perhaps magnetic field strengths, radii and masses) and thereby constrain the equation of state of ultra–dense matter, and to verify untested general relativistic effects by tracing space–time just above the neutron star surface (e.g. Kluzniak 1993; Miller, Lamb & Psaltis 1998; Kaaret, Ford & Chen 1997; Zhang, Strohmayer & Swank 1997; Zhang et al. 1998; Stella & Vietri 1998; Stella & Vietri 1999; Psaltis & Norman 2001). The discovery of kHz QPOs in GX 5–1 was reported by Wijnands et al. (1998). The HBOs were discovered by van der Klis et al. (1985), and the NBOs in GX 5–1 by Lewin et al. (1992). The source was also detected at radio (Braes, Miley & Schoenmakers 1972) and infrared wavelengths (Jonker et al. 2000a). In this paper we present an analysis of all *RXTE* observations of GX 5–1 obtained before 2001. We show for the first time the kHz QPO separation frequency is not constant in GX 5–1. We show that besides the two harmonically related low–frequency QPOs found previously on the Horizontal Branch, two additional harmonically related broad Lorentzian components are needed to obtain a good fit. We discuss the power spectra and colour–colour diagrams of the black hole candidate XTE J1550–564, the Z source GX 5–1, and the atoll source 4U 1608–52, and conclude that there are some remarkable similarities and differences which have not been appreciated in the past due to differences in analysis conventions between in particular neutron stars and black hole candidates.

2   OBSERVATIONS AND ANALYSIS

GX 5–1 was observed 76 times in the period spanning July 27 1996 to March 3 2000 with the proportional counter array (PCA: Jahoda et al. 1996) on board the *Rossi X–ray Timing Explorer (RXTE)* satellite (Bradt, Rothschild & Swank 1993). A log of the observations is presented in Table 1. The total observing time was $\sim$564 ksec. During $\sim$40% of the time only a subset of the 5 detectors was active. Two short observations (2 and 4) were omitted from our analysis due to data overflows. Data were always obtained in a mode providing 16 s time–resolution and a high spectral resolution (129 channels covering the effective 2–60 keV range; the Standard 2 mode). In addition, a variety of high time–resolution modes was used in the various observing campaigns; for all observations data with a time resolution of at least 2^{-11} s were obtained in the energy band spanning 2–60 keV.

From the Standard 2 data we computed HIDs. We only used data obtained with the two detectors (proportional counter units 0 and 2) that were always operational since each detector has a slightly different energy response. The background was subtracted using the standard PCA background subtraction model version 2.1e, where we used the version of the *skyvle* model appropriate for data from each epoch. The hardness, or hard colour, and intensity are defined as the logarithm of the 10.2–17.5 / 6.5–10.2 keV count rate ratio and as the count rate in the 2.5–17.5 keV band of a 16 s average, respectively (RXTE energy channels 25–44 / 14–24 and 3–44, respectively). The high voltage setting of the PCA detectors was changed on March 22 1999 (i.e., the gain changed). Combined with the finite energy resolution this forced us to use somewhat different energy boundaries in our computation of the HID for data obtained after March 22 1999 (i.e., 10.1–17.6 keV / 6.6–10.1 keV for the hard colour and 2.6–17.6 keV for the intensity for observations 42–76. We used RXTE energy channels 20–36 / 11–19 and 2–36, respectively). Besides the gain change the energy response of the detectors changed slowly with time. These various changes have been partially corrected for using the Crab pulsar as a reference, under the assumption that the spectrum of the Crab pulsar does not vary. This correction is only perfect if the spectral shape of GX 5–1 is equal to that of the Crab (the steps involved in this correction were outlined in Di Salvo et al. 2001 and Jonker et al. 2001). So, a small systematic error is introduced both by the correction for the drift in detector response and the slightly different energy boundaries which we used as a result of the gain change. Together with the secular variation of the source (Kuulkers, van der Klis & Vaughan 1996) this led us to compute 5 separate HIDs combining observations 1–7, 8–18, 19–26, 27–41, 42–76 (see Fig. 1 *left panel*; Table 1).

In Fig. 1 (*right panel*) the 5 HIDs are overplotted. The source was found on the Horizontal Branch, Normal Branch, and Flaring Branch in four of the five HIDs; for the HID of observations 42–76 the source was not found on the Horizontal Branch. The position of the source along the Z track is characterized by a parameter called S_z representing curve length along the track (Hasinger et al. 1990; Hertz et al.

**Table 1.** Log of the observations of GX 5–1 used in this analysis.

Obs. No.	Observation ID	Date & Start time (UTC)	Amount of good data (ksec)	Obs. No.	Observation ID	Date & Start time (UTC)	Amount of good data (ksec)
1	10257-05-01-00	21-07-1996 23:42	$\sim$ 0.14	39	30042-01-18-00	21-11-1998 22:35	$\sim$ 12.0
2	10257-05-02-00	24-10-1996 20:02	Omitted	40	30042-01-19-00	22-11-1998 06:35	$\sim$ 6.8
3	10061-02-01-00	02-11-1996 08:34	$\sim$ 14.5	41	30042-01-20-00	22-11-1998 09:47	$\sim$ 3.5
4	10063-01-01-00	03-11-1996 20:10	Omitted	42	40018-02-01-05	01-03-2000 14:26	$\sim$ 1.0
5	10063-02-01-00	03-11-1996 20:30	$\sim$ 10	43	40018-02-01-00	01-03-2000 23:29	$\sim$ 26.0
6	10061-02-02-00	06-11-1996 21:19	$\sim$ 14.8	44	40018-02-01-10	02-03-2000 04:29	$\sim$ 2.3
7	10061-02-03-00	16-11-1996 00:55	$\sim$ 15.4	45	40018-02-01-02	02-03-2000 06:16	$\sim$ 5.5
8	20055-01-01-00	15-02-1997 08:32	$\sim$ 4.8	46	40018-02-01-03	02-03-2000 12:14	$\sim$ 2.6
9	20055-01-02-00	12-04-1997 19:00	$\sim$ 4.8	47	40018-02-01-06	02-03-2000 14:05	$\sim$ 1.9
10	20055-01-03-00	29-05-1997 19:18	$\sim$ 5.3	48	40018-02-01-01	02-03-2000 15:28	$\sim$ 2.7
11	20053-02-01-00	30-05-1997 09:28	$\sim$ 17.6	49	40018-02-01-04	02-03-2000 17:11	$\sim$ 14.6
12	20053-02-01-04	06-06-1997 00:28	$\sim$ 5.2	50	40018-02-02-00	03-03-2000 00:00	$\sim$ 7.6
13	20053-02-02-00	25-07-1997 05:19	$\sim$ 9.2	51	40018-02-02-02	03-03-2000 07:24	$\sim$ 13.9
14	20053-02-01-02	25-07-1997 11:43	$\sim$ 13.1	52	40018-02-02-10	03-03-2000 13:48	$\sim$ 2.7
15	20053-02-01-03	25-07-1997 18:23	$\sim$ 5.2	53	40018-02-02-03	03-03-2000 23:23	$\sim$ 26.0
16	20053-02-01-01	25-07-1997 21:41	$\sim$ 8.3	54	40018-02-02-04	04-03-2000 05:56	$\sim$ 17.0
17	20055-01-04-00	28-07-1997 18:21	$\sim$ 4.8	55	40018-02-02-05	04-03-2000 13:51	$\sim$ 2.3
18	20055-01-05-00	21-09-1997 12:29	$\sim$ 4.6	56	40018-02-02-12	04-03-2000 15:37	$\sim$ 1.6
19	30042-01-01-00	22-08-1998 10:36	$\sim$ 11.3	57	40018-02-02-21	05-03-2000 00:57	$\sim$ 23.1
20	30042-01-02-00	14-09-1998 00:25	$\sim$ 2.8	58	40018-02-02-14	05-03-2000 04:14	$\sim$ 2.7
21	30042-01-03-00	25-09-1998 03:28	$\sim$ 9.6	59	40018-02-02-01	05-03-2000 06:07	$\sim$ 2.4
22	30042-01-04-00	08-10-1998 08:18	$\sim$ 4.6	60	40018-02-02-20	05-03-2000 12:02	$\sim$ 2.4
23	30042-01-02-01	09-10-1998 03:30	$\sim$ 5.7	61	40018-02-02-06	05-03-2000 13:43	$\sim$ 2.3
24	30042-01-05-00	14-10-1998 00:17	$\sim$ 10.5	62	40018-02-02-08	05-03-2000 15:19	$\sim$ 2.4
25	30042-01-06-00	26-10-1998 04:58	$\sim$ 9.7	63	40018-02-02-13	05-03-2000 16:58	$\sim$ 14.8
26	30042-01-07-00	30-10-1998 05:23	$\sim$ 5.9	64	40018-02-02-07	06-03-2000 00:57	$\sim$ 1.9
27	30042-01-08-01	02-11-1998 06:34	$\sim$ 3.0	65	40018-02-02-17	06-03-2000 02:33	$\sim$ 3.5
28	30042-01-08-00	03-11-1998 03:18	$\sim$ 11.9	66	40018-02-02-22	06-03-2000 04:09	$\sim$ 3.4
29	30042-01-09-00	04-11-1998 05:01	$\sim$ 6.1	67	40018-02-02-16	06-03-2000 05:45	$\sim$ 3.5
30	30042-01-10-00	08-11-1998 06:36	$\sim$ 2.7	68	40018-02-02-11	06-03-2000 07:17	$\sim$ 3.7
31	30042-01-11-01	08-11-1998 10:01	$\sim$ 1.3	69	40018-02-02-23	06-03-2000 09:07	$\sim$ 2.7
32	30042-01-11-00	09-11-1998 06:38	$\sim$ 8.6	70	40018-02-01-07	06-03-2000 10:30	$\sim$ 1.9
33	30042-01-12-00	10-11-1998 00:07	$\sim$ 10.3	71	40018-02-02-16	06-03-2000 13:40	$\sim$ 2.2
34	30042-01-13-00	10-11-1998 06:40	$\sim$ 11.2	72	40018-02-01-08	06-03-2000 15:16	$\sim$ 2.2
35	30042-01-14-00	11-11-1998 03:16	$\sim$ 10.4	73	40018-02-02-09	06-03-2000 16:52	$\sim$ 14.9
36	30042-01-15-00	20-11-1998 16:10	$\sim$ 5.4	74	40018-02-02-18	07-03-2000 00:53	$\sim$ 7.2
37	30042-01-16-00	21-11-1998 00:10	$\sim$ 23.4	75	40018-02-02-24	07-03-2000 04:04	$\sim$ 3.6
38	30042-01-17-00	21-11-1998 11:47	$\sim$ 13.9	76	40018-02-02-19	07-03-2000 05:38	$\sim$ 11.1

1992). The Z tracks were parametrized by fitting a spline through manually selected points along the track in each of the 5 HIDs separately. The S_z values are determined using the logarithm of the colours and count rate (Wijnands et al. 1997b) and normalized by assigning the hard vertex (the Horizontal Branch–Normal Branch junction) the value '1' and setting the soft vertex (the Normal Branch–Flaring Branch junction) to '2'. This defines the measure of curve–length, and therefore, $S_z = 0$ and $S_z = 3$ are not special points or vertices. We applied this parameterization to the HID obtained from each of the subsets. The track traced out by the source during observations 42–76 only covers part of the Z. In order to calculate the S_z values along this track we assumed that the hard vertex in that data set was at the same position relative to the soft vertex as in the HID of observations 27–41.

Using the high time–resolution data we calculated power–density spectra (2–60 keV) of data stretches of 16 s, up to a Nyquist frequency of 2048 Hz, using a Fast Fourier Transformation algorithm. The power spectra were normalized to fractional rms amplitude squared per Hz, added, and averaged according to their position along the Z track (the selection method will be described in detail below). Due to the relatively low amplitude of the variability in the high frequency part of the power spectrum, simultaneous fits of the entire frequency range would not constrain the properties of the high frequency part. Therefore, we fitted the low

(1/16–128 Hz) and high ($\sim$128–2048 Hz) frequency part of the power spectra separately. The low–frequency part of the average power spectra was fit with a function consisting of an exponentially cut–off power law to describe the noise at low frequencies (LFN) and at most five Lorentzians to fit the QPOs. The component arising in the power spectrum due to the Poisson counting noise was subtracted. For values of $S_z > 1.0$ a power law was added to the fit function to fit the very low–frequency noise (VLFN). The function used to describe the high–frequency part of the average power spectrum was built up out of two Lorentzians describing the kHz QPOs. Contrary to when we fit the low–frequency part, the continuum due to Poisson noise was not subtracted prior to fitting, therefore we included a constant to account for this Poisson noise. Sometimes also a power law component was added to account for the slope of the underlying continuum, caused by the high frequency tail of one of the low–frequency components. The high frequency tail did not systematically influence our fit–parameters.

From previous studies of GX 5–1 and other Z sources it is known that the frequency of the QPOs on the Horizontal Branch (the HBOs and the kHz QPOs) increases with S_z (Wijnands et al. 1998; Dieters & van der Klis 2000; Jonker et al. 2000b; Homan et al. 2001a). For all but the HID of observations 42–76 (when the source was not found on the Horizontal Branch or the upper part of the Normal Branch and therefore no HBOs were present in the power spectra;
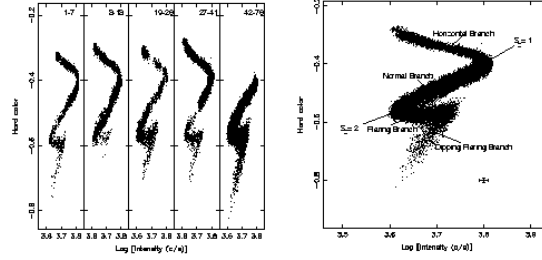
Figure 1. *Left panel:* Hardness–intensity diagrams for observations 1–7, 8–18, 19–26, 27–41, 42–76. *Right panel:* Hardness–intensity diagram of all observations combined. The hard colour is the logarithm of the 10.2–17.5/6.5–10.2 keV count rate ratio for observations 1–41 and that of the 10.1–17.6 / 6.6–10.1 keV count rate ratio for observations 42–76. The intensity is the 2.5-17.5 keV (observations 1–41), and the 2.6–17.6 keV (observations 42–76) count rate. The data were background–subtracted and corrected for changes in the energy response of the PCA detectors (see text), but no deadtime corrections were applied (the deadtime correction is <4%). Typical error bars (not including systematic errors) are shown at the bottom right of the figure in the right panel.

see Fig. 1 *left panel*) we studied the relation between S_z and HBO frequency. These relations, plotted in Fig. 2, have two notable properties. First, the relation found for observations 27–41 is clearly offset from the other relations. This is an effect of secular motion of the source during the gap in between the observations 27–35 and 36–41. During the first 9 observations (27–35) the source was found on the Horizontal Branch, whilst, after a 9 day gap, during observations 36–41 the source traced a part of the Horizontal Branch close to the Normal Branch, the Normal Branch, and the Flaring Branch. We checked the vertices of the 5 HIDs to search for additional evidence of secular motion but in view of the uncertainties involved in their manual selection, we conclude that the vertices of the 5 HIDs were not significantly different. The second notable property involves the jump in HBO frequency near $S_z \sim 1$ (see also plots in Wijnands et al. 1998). To investigate the nature of the jump further we plotted the hard colour vs. the frequency of the HBO. A discontinuity in the rate of change in frequency as a function of hard colour was also observed in the hard colour vs. frequency plot at a frequency of $\sim$50 Hz. Therefore, the jump in frequency when plotted vs. S_z is not an artefact of the S_z parameterization. We investigated whether a similar jump was present in the frequencies of the kHz QPOs, but we lacked the signal–to–noise to conclude on this.

In order to combine all power spectra with similar HBO frequencies, we shifted all S_z–HBO frequency relations to one "parent" relation. To this end, we fitted a polynomial to the relation between S_z and HBO frequency for each of the HIDs separately. We included only measurements

for $S_z < 1.0$ in the fit. The order of the polynomial was determined such that the reduced χ^2 of the fit was $\sim$1. The parent relation for $S_z < 1.0$ is the best linear fit to the S_z–HBO frequency relation for all the HIDs combined ($\nu_{HBO} = 9.9 + 36.8 \times S_{z,parent}$; the drawn line in Fig. 2). The shifting procedure works as follows: given the S_z value ($S_{z,\text{initial}}$) obtained from the HID corresponding to the observation the power spectrum is calculated from, the HBO will have a certain predicted frequency which follows from the S_z–HBO frequency relation found for that HID. That predicted HBO frequency corresponds, given the S_z–HBO frequency parent relation, to a $S_{z,\text{parent}}$. This $S_{z,\text{parent}}$ is then assigned to the power spectrum instead of $S_{z,\text{initial}}$ (the change of S_z corresponds to a horizontal shift in Fig. 2). This shifting procedure was done for each 16 s power spectrum separately. Finally, all power spectra were selected according to their $S_{z,\text{parent}}$ values for $S_z < 1.0$; the selection bin width was 0.1. For $S_z > 1.0$ the unshifted values obtained from each separate HID were used in the selection, since both the secular motion and the effects of the changes in the response move the Z track in a direction nearly perpendicular to the Normal Branch. Here the selected bin width was 0.05. The selected power spectra were averaged and fitted with the function described above.

The errors on the fit parameters were determined using $\Delta\chi^2 = 1.0$ (1σ, single parameter). The error on S_z is the standard deviation of the distribution of S_z values in one selection bin. In cases where components were not significantly detected, 95% confidence upper limits were determined using $\Delta\chi^2 = 2.71$. The full–width at half maximum (FWHM)
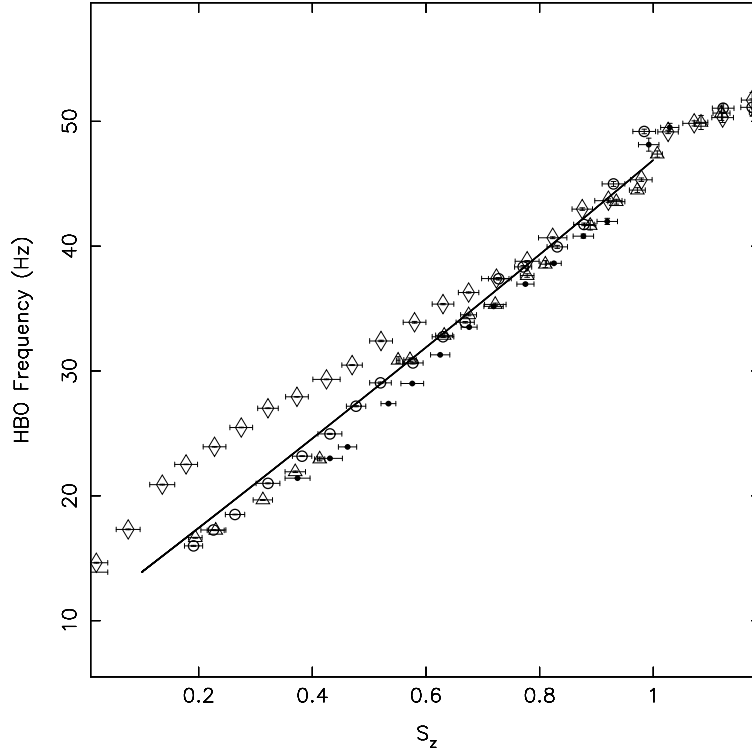
Figure 2. The S_z–HBO frequency relation measured for four different HIDs. The S_z–HBO frequency relation found for the HID of the observations 27–41 (diamonds) is clearly offset with respect to the relations found for the other HIDs (dots represent observations 1–7, open circles observations 8–18, and triangles observations 19–26). The drawn line is the parent relation to which all the relations are scaled (see text). Error bars are shown for each measurement; the error on the HBO frequency is in most cases smaller than the size of the symbols.

of the Lorentzians was fixed at 10 Hz in case an upper limit was determined to the sub–HBO, its third harmonic or the second harmonic of the HBO, and at 30 Hz in case of the first harmonic (which is the fundamental) of the HBO. The frequency of the component for which an upper limit was determined was not fixed but restricted to a range of values around that expected on the basis of the observed trends. Upper limits to the presence of kHz QPOs were determined using a FWHM of 75 Hz.

3   RESULTS

3.1   Spectral states

The source was found on the Horizontal Branch, Normal Branch and Flaring Branch. Note the clear "Dipping Flaring Branch" trailing the Flaring Branch (see Fig. 1, see also Kuulkers et al. 1994). GX 5–1 was found to reside most often on the Normal Branch during the time of our observations (see Fig. 3, *upper panel*). The average velocity along the Z track (defined as the average of $V_z(i) = \frac{S_z(i+1)-S_z(i-1)}{T(i+1)-T(i-1)}$; Wijnands et al. 1997b; Fig. 3, *lower panel*) was approximately constant for $0.1 < S_z < 1$ but gradually increased for $S_z > 1$, i.e., in anti–correlation with the time the source spent in each part of the Z diagram, although the product of the two is not exactly constant. Note that the average velocity along the Z track also increased towards the lowest S_z values.

3.2   Low–frequency power spectra

We found two new components in the averaged power spectrum of GX 5–1. One of these components was located at frequencies consistent with half the frequency of the HBO, the so–called sub–HBO. This component was reported before in the Z sources Sco X–1, GX 340+0, and GX 17+2 with RXTE (Wijnands & van der Klis 1999; Jonker et al. 2000b; Homan et al. 2001a). The second new component has a frequency which is consistent with three times the frequency of the sub–HBO (or 1.5 times the frequency of the HBO; see Fig. 4). Fitting the average low–frequency (1/16–256 Hz) power spectrum of $S_z = 0.60 \pm 0.03$ with a function consisting of a cut–off power law (LFN), and three Lorentzians (sub–HBO, HBO, and 2nd harmonic of the HBO) a χ^2 of 383 for 209 degrees of freedom was obtained. Adding a fourth Lorentzian component at frequencies ∼3 times the frequency of the sub–HBO gave a χ^2 of 314 for 206 degrees of freedom. An F–test (Bevington & Robinson 1992) to the χ^2 of the fits with and without the fourth Lorentzian revealed that the probability that the reduction in χ^2 could be achieved by a random process is 6.5×10^{-8}, i.e., the significance of the addition of the fourth Lorentzian component is ∼ 6σ. For the other power spectra where this component was found a similar value was obtained. Although this component is too broad to qualify formally as a QPO (since the Q–value is less than 2; see Table 2 and Fig. 4, *right panel*), for now we refer to this component as the third harmonic to the sub–HBO component (see Fig. 4). This classification is rendered
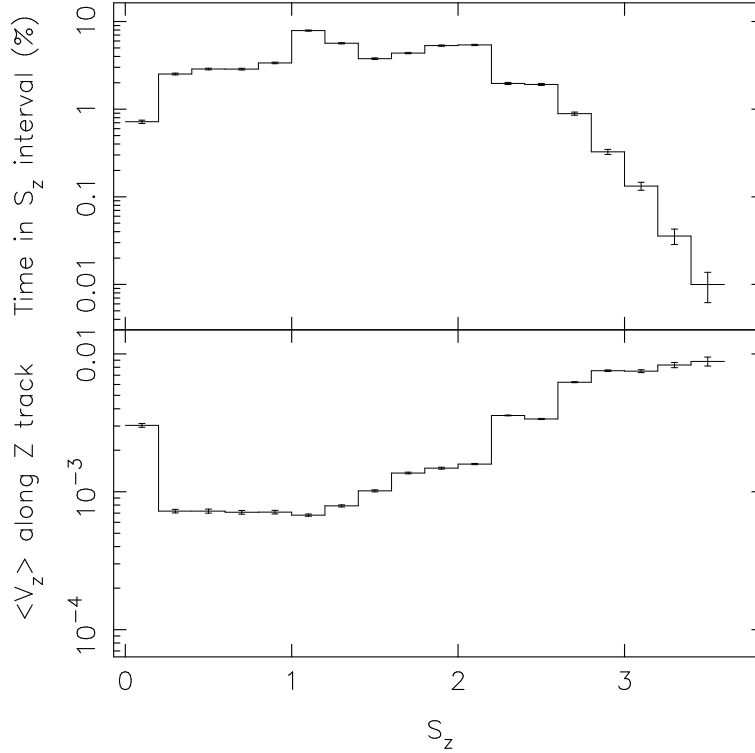
Figure 3. *Upper panel:* Percentage of the total observing time spent in each S_z interval as a function of the S_z value. During our observations the source spent most of the time on the Normal Branch (S_z values between 1 and 2). *Lower panel:* The average velocity (see text) of the source along the Z track. The average velocity was approximately constant for $S_z < 1$ (except towards the lowest S_z values where it increased) but steadily increased for $S_z > 1$.

strong support by the fact that the Q–values of both the sub–HBO and its third harmonic are consistent with being the same (Fig. 4; *right panel*).

Similar to our work on the Z–source GX 340+0 (Jonker et al. 2000b) we also experimented with several other fit functions used by various authors to describe the power spectra of other LMXBs. Both using a fit function built up out of a broken power law, to fit the LFN component, and several Lorentzians to fit the QPOs, and a fit function built up out of just Lorentzians resulted in significantly higher χ^2_{red} values than when the fit function described in above was used (χ^2_{red}= 2.67 for 207 degrees of freedom (d.o.f.), and χ^2_{red}= 1.93 for 205 d.o.f., respectively), while adding the fourth Lorentzian component to these fit functions still improved the χ^2_{red} significantly (to χ^2_{red}= 2.48 for 204 d.o.f., and χ^2_{red}= 1.73 for 202 d.o.f., respectively).

Besides the two new components, the HBO, its second harmonic and the LFN were also detected (see Table 2, 3). A typical fit ($S_z = 0.60 \pm 0.03$) showing the contributions of the individual components is presented in Fig. 5. In four of the S_z selections the HBO was fit with two Lorentzian peaks in order to obtain a good fit (see Table 2). This is either related to the fact that the HBO moves in frequency within the selection, or the HBO profile itself is asymmetric. Whenever two Lorentzian peaks were used to describe the HBO we obtained the rms and FWHM weighted mean of the two peaks; we used the weighted mean parameters in Fig. 4 and in Table 2. We weighted the frequencies according to one over the square of the FWHM and proportionally to the square of the amplitude. The FWHMs were weighted pro-

portionally to the square of the amplitude. The frequency offsets between the two peaks were ignored in the weighing since one of the two Lorentzian peaks contained several times more power than the other. The powers of the two Lorentzians were added. We would like to remark that the jump in HBO frequency vs. S_z for each HID (Fig. 2) has been reduced due to the shifting to $S_{z,parent}$.

The fractional rms amplitude (integrated between frequencies ranging from $0–\infty$) of all the low–frequency Lorentzian components (excluding the NBO) decreased as a function of S_z (see Fig. 6 upper panels; Table 2). For $S_z = 1.0 − 1.5$ the frequency and the fractional rms amplitude of the HBO was consistent with being constant at ~ 50 Hz and $\sim 2\%$, respectively. For $S_z > 1.5$ the HBO was not detected with an upper limit of 1.2%. The FWHM of the Lorentzian components increased as a function of S_z (see Fig. 6 lower panels; Table 2).

The fractional rms amplitude of the LFN (0.1–100 Hz) decreased from 7.4%±0.3% to 3.38%±0.02% as S_z increased from 0.12±0.03 to 1.01±0.02 (Table 3). The LFN component could not be measured for $S_z > 1$. The LFN power law index increased from 0.07±0.05 to 0.41±0.01 while the cut–off frequency increased from 2.9±0.5 Hz to ~ 60 Hz. For $S_z > 1$ we added a power law to the fit function to represent the power at frequencies below 1 Hz; the very low–frequency noise (VLFN). The VLFN fractional rms amplitude (0.001–1 Hz) increased from less than 1% at the hard vertex to more than 20% at $S_z > 3.0$. This increase was gradual for $S_z < 2.0$ but steep for $S_z > 2.0$ (see Fig. 7, Table 3). The VLFN power law index gradually increased to 1.5 and re-
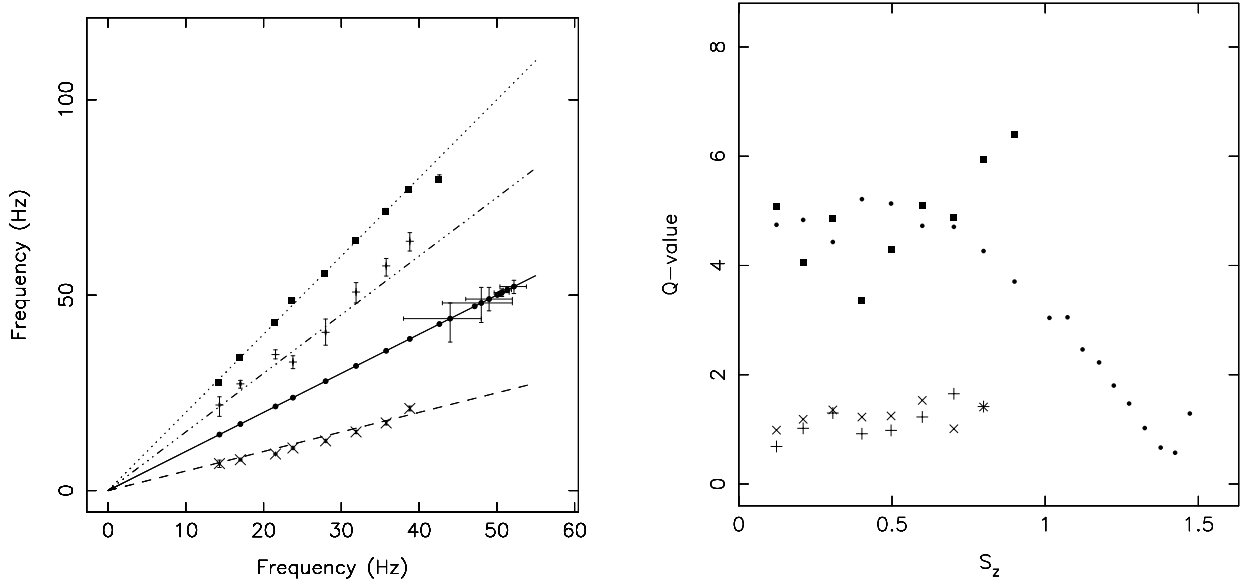
Figure 4. *Left panel:* The frequencies of the four Lorentzian components used to fit the average power spectra for $S_z < 1.5$, plotted against the frequency of the HBO. The lines represent 0.5 (dashed line overlaying the crosses), 1.0 (drawn line overlaying the filled circles), 1.5 (dashed–dotted line overlaying the plus symbols), and 2.0 (dotted line overlaying the squares) times the HBO frequency. Error bars are plotted but in several cases they are smaller than the size of the symbols. *Right panel:* The Q–values of the 4 harmonics. The HBO and its second harmonic have Q–values near 5 over the range where they are detected simultaneously, thereafter the HBO coherence drops steadily. The Q–values of the sub–HBO and its third harmonic are around 1, with only a slight increase between $S_z \sim 0.1$ and $S_z \sim 0.8$. Error bars are omited for clarity but they are a few times larger than the size of the symbols. The same symbols as in the *left panel* have been used.
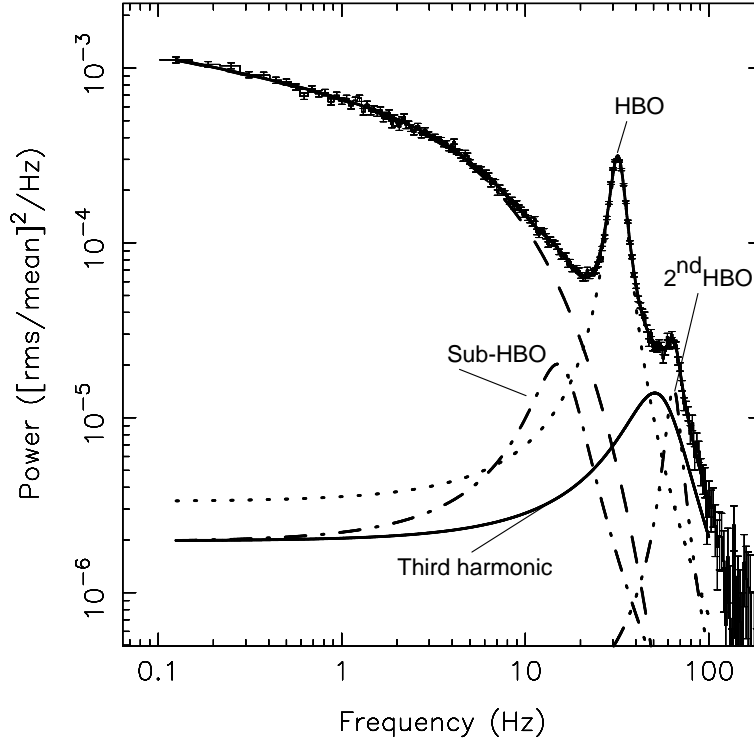
Figure 5. Average 2–60 keV power density spectrum for $S_z = 0.60 \pm 0.03$. The best–fitting and the individual components used in this fit are indicated; the dashed line represents the LFN, the dotted line the HBO, the dash–dot line the sub–HBO, the solid line its third harmonic, and the dash–three dots line the second hamonic of the HBO. The component arising in the power spectrum due to Poisson noise was subtracted.

Table 2. Best–fitting parameters of the Lorentzian components of the low frequency power spectra (2–60 keV) as a function of S_z.

| S_z value[c]	Sub frac. rms amp. %	FWHM sub (Hz)	Freq. sub (Hz)	HBO frac. rms amp. %	FWHM HBO (Hz)	Freq. HBO (Hz)	2^{nd}_{HBO} frac. rms amp. %	FWHM 2^{nd}_{HBO} (Hz)	Freq. 2^{nd}_{HBO} (Hz)	3^{rd}_{sub} frac. rms amp. %	FWHM 3rd (Hz)	Freq. 3rd (Hz)
0.12±0.03	$2.5^{+1.7}_{-0.8}$	7±3	7±1	7.8±0.5[b]	3.0±0.2[b]	14.33±0.05[b]	1.9±0.6	6 ±2	27.9±0.3	5.0±0.3	32±4	22±3
0.21±0.03	3.0±0.2	6.7±0.4	7.9±0.2	7.7±0.2[b]	3.5±0.1[b]	17.02±0.08[b]	1.7±0.1	9 ±1	34.4±0.2	4.3±0.1	27±1	27±1
0.31±0.03	2.7±0.2	6.9±0.5	9.4±0.2	7.24±0.03	4.9±0.1	21.53±0.01	1.7±0.3	9 ±2	43.2±0.3	3.4±0.1	27±1	35±1
0.40±0.03	2.5±0.2	8.9±0.7	10.9±0.2	6.38±0.07[b]	4.6±0.1[b]	23.78±0.05[b]	2.1±0.2	15±2	48.8±0.3	3.5±0.2	36±2	33±2
0.50±0.03	2.1±0.2	10±1	12.7±0.3	5.9±0.2 [b]	5.5±0.2[b]	27.98±0.06[b]	1.9±0.2	13±2	55.7±0.2	2.8±0.2	41±2	41±3
0.60±0.03	1.6±0.2	10±1	15.0±0.4	5.45±0.04	6.8±0.1	31.90±0.02	1.6±0.2	13±2	64.2±0.3	2.6±0.1	41±3	51±3
0.70±0.03	2.1±0.2	17±2	17.3±0.6	4.66±0.03	7.6±0.1	35.77±0.03	1.5±0.3	15±3	71.7±0.5	2.2±0.3	35^{+3}_{-10}	58±2
0.80±0.03	1.3±0.3	15±3	21.0±0.6	4.02±0.03	9.1±0.1	38.81±0.03	1.1±0.2	13±4	77.2±0.6	2.2±0.1	45±3	64±2
0.90±0.03	<0.6	10[a]	....	3.19±0.02	11.5±0.2	42.61±0.05	0.8±0.1	13±4	79.9±0.9	<0.9	10[a]	....
1.01±0.03	<0.5	10[a]	....	2.81±0.02	15.5±0.3	47.14±0.08	<0.4	10[a]	....	<0.7	10[a]	....
1.07±0.02	....	....	....	2.37±0.02	16.4±0.4	50.0±0.1	....	....	....	....	....	....
1.12±0.02	....	....	....	2.18±0.03	20.4±0.8	50.2±0.2	....	....	....	....	....	....
1.18±0.02	....	....	....	1.95±0.04	23±1	50.5±0.3	....	....	....	....	....	....
1.22±0.02	....	....	....	1.69±0.07	29±3	51.3±0.5	....	....	....	....	....	....
1.27±0.02	....	....	....	1.66±0.09	34±4	51±1	....	....	....	....	....	....
1.33±0.02	....	....	....	1.7±0.1	51±9	52±2	....	....	....	....	....	....
1.38±0.02	....	....	....	1.7±0.2	72±15	48±5	....	....	....	....	....	....
1.42±0.02	....	....	....	1.7±0.2	77±15	44±5	....	....	....	....	....	....
1.47±0.02	....	....	....	1.4±0.2	38±11	49±3	....	....	....	....	....	....

[a]Parameter fixed at this value [b]Parameter is the weighted average of two Lorentzians (see text) [c]The error on S_z is the standard deviation of the distribution of S_z values in the selection bin

Table 3. Best–fitting parameters of the cut–off power law, the power law, and the NBO component of the low frequency power spectra (2–60 keV) as a function of S_z.

S_z value[c]	LFN frac. rms amp. %	Power law index	Cut–off freq. (Hz)	VLFN frac. rms amp. %	Power law index	NBO frac. rms amp. %	FWHM NBO (Hz)	Freq. NBO (Hz)
0.12±0.03	7.4±0.3	7e-2±5e-2	2.9±0.5	....	....	....	....	....
0.21±0.03	7.57±0.06	2e-2±1e-2	2.97±0.1	....	....	....	....	....
0.31±0.03	7.29±0.06	1e-2±2e-2	3.43±0.1	....	....	....	....	....
0.40±0.03	7.06±0.06	7e-2±1e-2	4.32±0.2	....	....	....	....	....
0.50±0.03	6.83±0.05	0.11±1e-2	5.4±0.2	....	....	....	....	....
0.60±0.03	6.48±0.05	0.20±1e-2	7.4±0.3	....	....	....	....	....
0.70±0.03	5.42±0.07	0.26±1e-2	8.7±0.5	....	....	....	....	....
0.80±0.03	4.81±0.09	0.37±1e-2	15±1	....	....	....	....	....
0.90±0.03	4.65±0.02	0.48±1e-2	68±2	< 0.4	1[a]	<0.4	10[a]	....
1.01±0.03	3.38±0.02	0.41±1e-2	59±2	< 0.5	1[a]	<0.7	10[a]	....
1.07±0.02	< 0.5	0.4[a]	....	0.92±0.07	1.0±0.1	$1.69^{+0.05}_{-0.09}$	14.4±0.9	6.1±0.3
1.12±0.02	< 0.5	0.4[a]	....	1.0±0.1	1.1±0.1	1.80±0.04	9.1±0.4	6.03±0.09
1.18±0.02	....	....	....	1.0±0.2	1.3±0.1	2.04±0.02	7.0±0.2	5.97±0.05
1.22±0.02	....	....	....	1.3±0.3	1.4±0.1	2.14±0.02	5.7±0.1	5.79±0.04
1.27±0.02	....	....	....	3.1±0.1	1.9[a]	2.35±0.02	4.8±0.1	5.67±0.03
1.33±0.02	....	....	....	$1.7^{+0.6}_{-0.4}$	1.6±0.2	1.9±0.1	2.7±0.2	5.25±0.05
1.38±0.02	....	....	....	1.4±0.3	1.4±0.1	2.0±0.2	2.3±0.2	5.33±0.06
1.42±0.02	....	....	....	1.8±0.4	1.5±0.1	2.23±0.08	2.6±0.1	5.43±0.04
1.47±0.02	....	....	....	2.6±0.1	1.6[a]	2.1±0.1	2.3±0.2	5.48±0.04
1.52±0.02	....	....	....	2.2±0.5	1.5±0.1	2.38±0.03	3.3±0.1	5.75±0.04
1.58±0.02	....	....	....	2.2±0.1	1.5[a]	2.17±0.03	3.7±0.2	5.92±0.05
1.63±0.03	....	....	....	2.1±0.1	1.5[a]	2.00±0.03	4.0±0.2	6.01±0.05
1.68±0.02	....	....	....	1.9±0.3	1.3±0.1	1.84±0.04	4.2±0.2	6.07±0.06
1.73±0.03	....	....	....	2.5±0.4	1.5±0.1	1.61±0.02	4.3±0.3	6.09±0.08
1.82±0.03	....	....	....	3.0±0.2	1.5±0.1	1.30±0.03	6.2±0.5	6.2±0.1
1.95±0.05	....	....	....	2.8±0.2	1.5±0.1	1.14±0.05	8.1±0.8	5.8±0.2
2.05±0.05	....	....	....	1.6±0.1	1.1±0.1	1.68±0.07[b]	-0.9±0.2[b]	4.3±0.6[b]
2.15±0.05	....	....	....	4.2±0.2	1.8[a]	2.07±0.05[b]	0.3±0.1[b]	18±3[b]
2.36±0.08	....	....	....	11±2	2.0±0.1	1.64±0.05[b]	0.4±0.1[b]	25±5[b]
2.64±0.06	....	....	....	17±2	1.9±0.1	1.54±0.07[b]	0.2±0.1[b]	25^{+8}_{-5} [b]
2.90±0.08	....	....	....	18±2	1.8±0.1	<1.2	0.3[a]	....
3.13±0.15	....	....	....	22±3	1.9±0.1	....	....	....

[a] Parameter fixed at this value [b] Fitted with a cut–off power law, FWHM stands for power law index, frequency stands for cut–off frequency [c] The error on S_z is the standard deviation of the distribution of S_z values in the selection bin
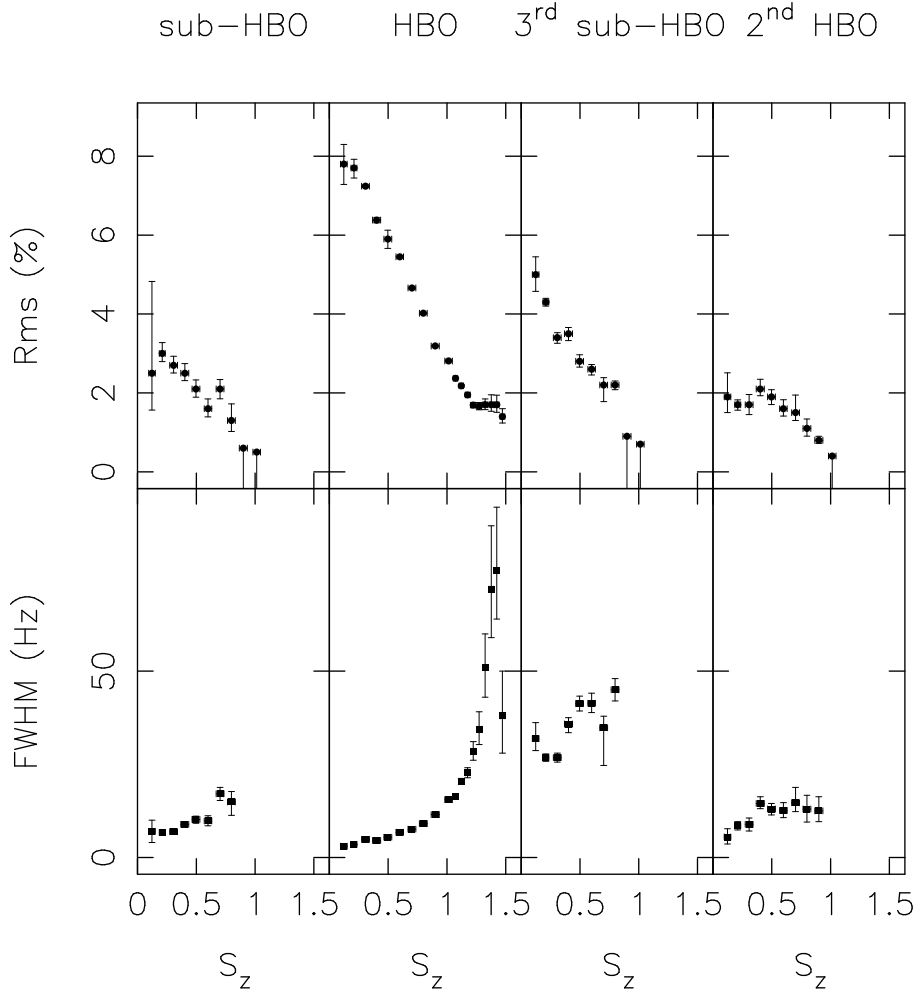
Figure 6. The fractional rms amplitude (2–60 keV; top panel) and the FWHM (bottom panel) of the sub–HBO, the HBO, the third harmonic of the sub–HBO, and the second harmonic of the HBO as a function of S_z. Error bars are plotted but may be smaller than the size of the symbols. Upper limits on the fractional rms amplitude of components are plotted using symbols without a positive error bar. The negative error bar extends to below zero.

mained constant for $S_z < 2.0$, for $S_z > 2.0$ the power law index was consistent with 2.

The frequency of the NBO decreased from 6.1±0.3 Hz at $S_z = 1.07 \pm 0.02$ to 5.25±0.05 Hz at $S_z = 1.33 \pm 0.02$ before it increased again to 6.1±0.1 Hz at $S_z = 1.82 \pm 0.03$. For $S_z > 1.9$ its frequency could not be determined with high accuracy since the FWHM increased to 8 Hz. The fractional rms amplitude of the NBO varied between $1.69\%^{+0.05}_{-0.09}\%$ and $2.38\%\pm0.03\%$ for $S_z = 1.07 \pm 0.02$ and $S_z = 1.52 \pm 0.02$, respectively but it decreased to $\sim$1.14%±0.05% at $S_z = $ 1.95±0.05. The somewhat erratic behaviour in the fractional rms amplitude of the NBO between $S_z = 1.3 - 1.5$ can be explained by the fact that the HBO was very broad and had power in the same frequency range as the NBO. The fractional rms amplitude is anti–correlated with the frequency and FWHM of the NBO (see Fig. 8). At $S_z < 1.0$ stringent upper limits on the presence of the NBO were derived.

At $S_z > 2.0$ the NBO was not detected but instead a cut–off power law was fitted to represent the power at frequencies comparable to the NBO frequencies. This cut–off power law was peaked (power law index of -0.9 ± 0.2) near the soft vertex, with power law index -0.9 ± 0.2 and evolved into

a flat–topped noise component at $S_z = 2.15 \pm 0.05$ with a typical power law index of 0.3. The cut–off frequency increased from 4.3±0.6 Hz to 25^{+8}_{-5} Hz. The fractional rms amplitude (0.001-100 Hz) increased from 1.68%±0.07% at $S_z = 2.05 \pm 0.05$ to 2.07%±0.05% at $S_z = 2.15 \pm 0.05$. For $S_z > 2.15$ the fractional rms amplitude was consistent with 1.6%. The noise component became undetectable at an S_z value of 2.64±0.06 with an upper limit of 1.2%, where the vertex between the Flaring Branch and the "Dipping Flaring Branch" is at $S_z \sim 2.5$. The fit parameters of the cut–off power law are marked with a ^{b} in Table 3.

3.3 KHz QPOs

The lower and upper kHz QPO were detected at frequencies ranging from 156±23 Hz to 627^{+25}_{-13} Hz and from 478±15 Hz to 866±23 Hz, respectively (dots and crosses, respectively *top panel*, Fig. 9 A). The peak separation ($\Delta\nu$) was not constant; the fit of a constant to the peak separation (325±10 Hz) vs. S_z resulted in a χ^2_{red} of 7 for 10 degrees of freedom; an unacceptable fit. We tried various other functions (e.g. see Fig. 9 *bottom panel* and Table 5). From an F–test it was
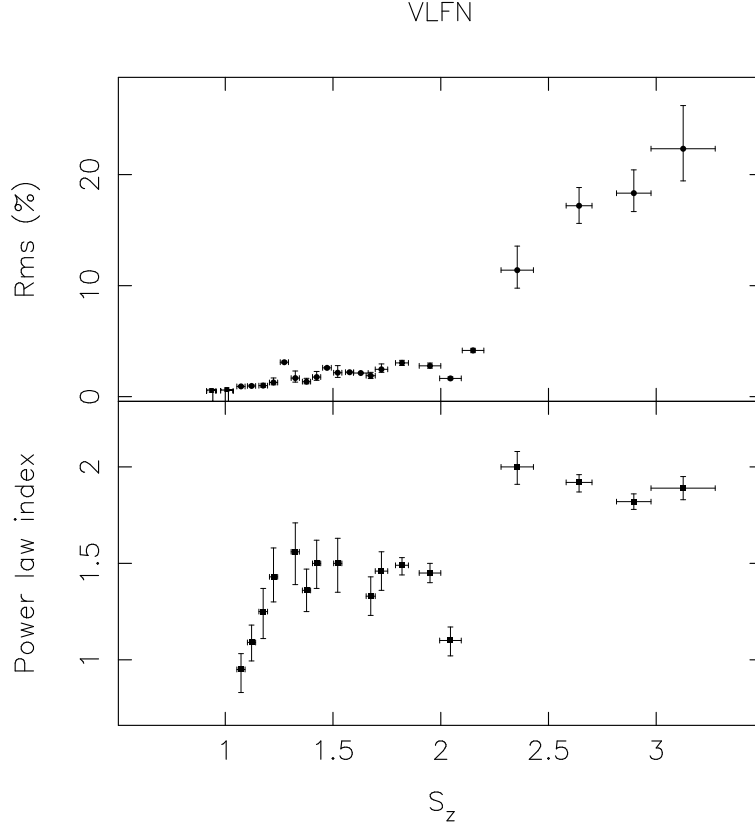
Figure 7. The fractional rms amplitude (2–60 keV; top panel) and power law index (bottom panel) of the VLFN as a function of S_z. Error bars are plotted but may be smaller than the size of the symbols.

clear that the use of a broken function or a parabola significantly reduced the χ^2 ($\sim 3.5\sigma$, $\sim 3\sigma$, respectively) with respect to a constant, indicating that $\Delta\nu$ is decreasing towards higher S_z at a rate that is not constant but increases. The data indicate a decrease in FWHM of the lower kHz QPO towards larger S_z, but the scatter is large. The FWHM of the upper kHz QPO varies between 100 Hz and 247 Hz (see crosses Fig. 9 B *top panel*). The fractional rms amplitude of the lower kHz QPO decreased gradually from 3.6%±0.4% to 0.5%±0.1%, that of the upper kHz QPO first increased slightly from 2.0%±0.4% to 2.6%±0.1% to decrease gradually to 0.9%± 0.1% (see dots and crosses respectively, Fig. 9 C *top panel*). The S_z changed from $\sim 0.1 - 1.1$ over the plotted interval. All fit results are given in Table 4.

Motivated by the results on GX 17+2 (Homan et al. 2001a) we plotted the frequency of the kHz QPOs and their separation frequency as a function of ν_{HBO} (Fig. 10). Near $\nu_{HBO} \sim 45$ Hz the peak separation starts to decrease most likely due to an increase in the rate at which the frequency of the lower kHz QPO increases with ν_{HBO}. This ν_{HBO} is consistent with the jump at $\nu_{HBO} \sim 44 - \sim 47$ Hz in a ν_{HBO} vs. S_z plot (see Section 2).

4   DISCUSSION

A detailed analysis of all *RXTE* observations obtained to date of GX 5–1 was presented. The main result of our high–frequency variability study is that the kHz QPO peak separation is not constant in GX 5–1. The low–frequency

power spectra for $S_z < 1.0$ are complex and can be best described by 4 harmonically related Lorentzians, in addition to the low–frequency noise (LFN). Two of these Lorentzians were not known previously in GX 5–1. At $S_z > 1.9$ a new component was found in the power spectra. Below we discuss these findings and compare the timing properties and colour–colour diagrams of GX 5–1, the black hole candidate XTE J1550–564, and the atoll source 4U 1608–52.

4.1   KHz QPOs

We showed that the kHz QPO peak separation is not constant. The data is consistent with a constant peak separation followed by a steep decrease for $S_z \sim 1.0$, or a parabolic relation between the peak separation and S_z. A decrease in peak separation was previously found in Sco X–1 (van der Klis et al. 1997), 4U 1608–52 (Méndez et al. 1998), 4U 1728–34 (Méndez & van der Klis 1999), 4U 1735–44 (Ford et al. 1998), 4U 1702–43 (Markwardt, Strohmayer & Swank 1999), and GX 17+2 (Homan et al. 2001a). We found that in GX 5–1 the rate of increase in frequency of the lower kHz QPO changes near $\nu_{HBO} \sim 45$Hz, causing the peak separation to decrease.

The frequencies of the kHz QPOs of GX 5–1 are low in comparison with the other kHz QPO Z sources (the lowest frequencies of the lower and upper kHz QPO we found are 156 ± 23 Hz, and 478 ± 15 Hz, respectively). The lowest upper kHz QPO frequency found so far in an atoll source (449 ± 20 Hz for 4U 0614+09; van Straaten et al. 2000) is at
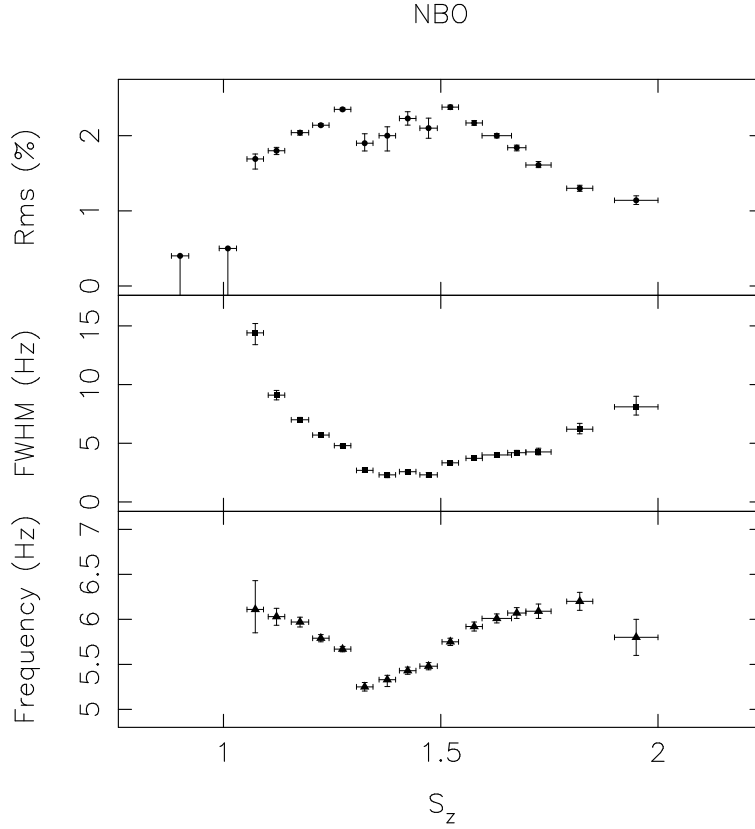
Figure 8. The fractional rms amplitude (2–60 keV; top panel), FWHM (middle panel), and frequency (bottom panel) of the NBO as a function of S_z. Error bars are plotted but may be smaller than the size of the symbols. Upper limits on the fractional rms amplitude of the NBO are plotted using symbols without a positive error bar. The negative error bar extends to below zero.

the low–frequency limit ($\sim$500 Hz for the upper kHz QPO; Miller, Lamb & Psaltis 1998) imposed by the sonic point beat frequency model. The cause of the lower bound on the Keplerian frequency in the sonic point beat frequency model is that the radiation drag of the luminosity produced near the surface of the neutron star can only remove the required amount of the specific angular momentum of the gas to make it fall to the neutron star when the gas is close to the neutron star (Miller, Lamb & Psaltis 1998). Unlike 4U 0614+09, in the case of GX 5–1 QPOs with still lower frequency did not occur because the source was not found at lower S_z values but not because the QPO disappeared. Therefore, observations of kHz QPOs in GX 5–1 at even lower S_z values will provide a strong test of the sonic point beat frequency model.

In the so–called two–oscillator model (Titarchuk, Lapidus & Muslimov 1998; Osherovich & Titarchuk 1999) the angle δ is de-fined ($\delta = arcsin[(\nu_{upper}^2 - \nu_{lower}^2)^{-0.5}(\nu_{HBO}\nu_{upper}/\nu_{lower})]$), where ν_{lower} is the frequency of the lower kHz QPO, ν_{upper} is the frequency of the upper kHz QPO, and ν_{HBO} is the frequency of the HBO; δ is the angle between the magneto-sphere equator and the disc plane in the model). The current version of the theory predicts δ to be constant. However, the measurements of Homan et al. (2001a) for GX 17+2 and the our measurements for GX 5–1 show that δ vs. the frequency of the lower kHz QPO changes is not constant (see Fig. 11). A fit of a constant gives $\delta = 6.1 \pm 0.2$ and a χ^2 of 377 for 9

d.o.f. for GX 17+2 and $\delta = 6.3 \pm 0.1$ and a χ^2 of 95.2 for 9 d.o.f. for GX 5–1.

4.2 Comparison with other Z sources

We have detected a sub–HBO component similar to the component in the Z–sources Sco X–1 (Wijnands & van der Klis 1999), GX 340+0 (Jonker et al. 2000b), and GX 17+2 (Homan et al. 2001a). Furthermore, we found a fourth Lorentzian component whose frequency was consistent with 1.5 times the frequency of the HBO. If we interpret the sub–HBO as the fundamental frequency, then the HBO would be the second harmonic, the newly found peak at 1.5 times the HBO frequency the third harmonic, and the second har-monic of the HBO the fourth harmonic. In such a scheme the odd harmonics should either be formed less coherently than the even harmonics, or an additional broadening mech-anism has to be invoked which broadens the odd harmonics more than the even harmonics (see Fig. 4; *right panel*). This harmonic structure could be explained in a scenario where the HBO is caused by a warped accretion disc with a two–fold symmetry. The warp itself is stable to deviations from its two–fold symmetry, i.e., variations in the warp take place on a timescale long compared to the timescale of variations in the difference between the two sides of the warp, lead-ing to broader odd harmonics. This connects to the models proposed by Stella & Vietri (1998) and Psaltis & Norman (2001). In the magnetic beat–frequency model for the HBO
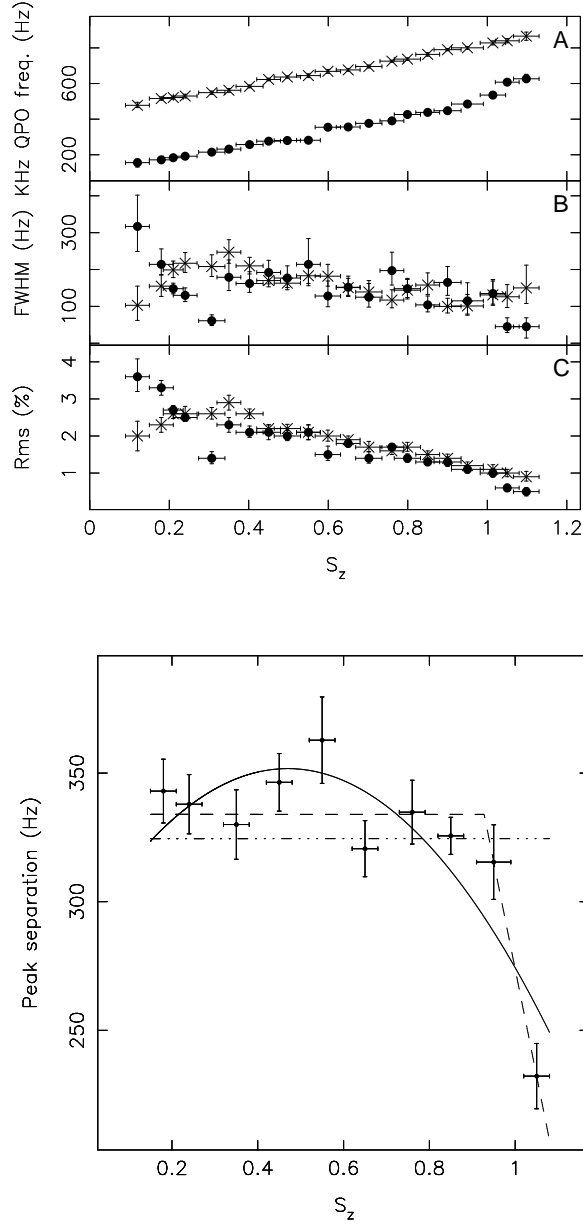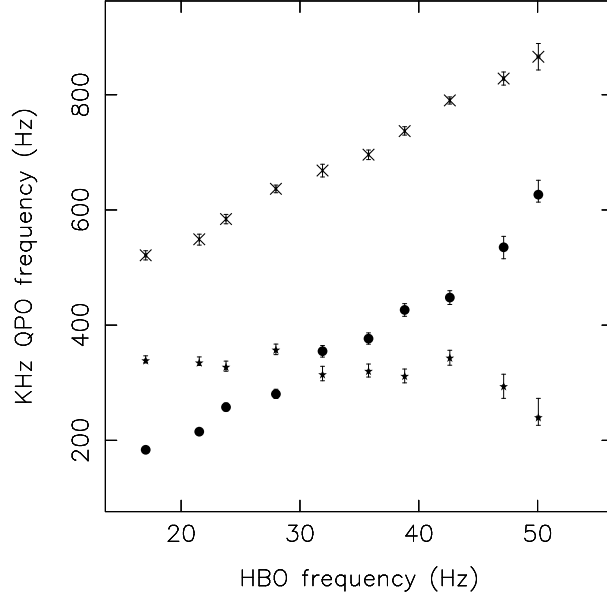
Figure 9. The kHz QPO properties as a function of S_z. The measurements presented in the *top panel* are dependent points since data have been used from partially overlapping bins. (*Top panel A:* The frequencies of the lower (dots) and upper kHz QPO (crosses), the same symbols for the lower and upper kHz QPO are used throughout the figure. *Top panel B:* The FWHM of the kHz QPO pair. *Top panel C:* The fractional rms amplitude (2–60 keV) of the kHz QPO pair. *Bottom panel:* The peak separation as a function of S_z. The dashed–dotted line represents the best–fitting constant, the drawn line represents the fit to the data of a parabola, and the dashed line represent a fit using two straight lines joined at the break with slope fixed to zero below the break at $S_z \sim 0.93$ (for the fit parameters see Table 5). Error bars are plotted, but the errors in the *top panel* can be smaller than the size of the symbols.

(Alpar & Shaham 1985; Lamb et al. 1985) the sub–HBO should reflect differences between the two magnetic poles. Differences in the magnetic field configuration are not likely to vary in time rapidly, so the extra broadening of the sub–HBO with respect to the HBO is unexplained. This necessitates the introduction of an additional broadening mechanism working on the odd harmonics only after their formation.

Prior to the detection of the sub–HBO and its third harmonic, the frequency of the second harmonic of the HBO was not measured to be exactly twice the HBO frequency (Wijnands et al. 1998); with the introduction of the third harmonic of the sub–HBO in the fit function this discrepancy has disappeared (see Fig. 4; *left panel*). Power density spectra calculated from data obtained with the EXOSAT and Ginga satellites (Kuulkers et al. 1994; Lewin et al. 1992) were fit using only the even harmonics (the HBO and its 2nd harmonic) and an additional high frequency noise (HFN) component. Now, using the larger collecting area of RXTE we find that the HFN in GX 5–1 is better described by two

Figure 10. The kHz QPO properties as a function of the HBO frequency. The dots represent the lower kHz QPO and the crosses the upper kHz QPO. The frequency of the peak separation is indicated with stars. The rate of increase in lower kHz QPO frequency and therefore also in the peak separation frequency changes near $\nu_{HBO} \sim 45$ Hz.

Table 4. Best–fitting parameters (2–60 keV) of the lower (ν_{low}) and upper (ν_{up}) kHz QPO as a function of the source position along the Z track. Note that overlapping selections in S_z have been used.

S_z value[a]	Fractional rms ampli. ν_{low}	FWHM lower kHz QPO (Hz)	Frequency lower kHz QPO (Hz)	Fractional rms ampli. ν_{up}	FWHM upper kHz QPO (Hz)	Frequency upper kHz QPO (Hz)
0.12±0.03	3.6±0.4	317±77	156±23	2.0±0.4	103±47	478±15
0.18±0.03	3.3±0.2	214±36	172±10	2.3±0.2	155±29	515±9
0.21±0.03	2.7±0.1	148±15	183±3	2.6±0.1	199±23	521±8
0.24±0.03	2.5±0.1	130±19	192±4	2.6±0.2	217±27	530±10
0.31±0.03	1.4±0.2	61 ±15	215±4	2.6±0.2	208±30	549±10
0.35±0.03	2.3±0.2	179±42	232±7	2.9±0.2	247±32	562±11
0.40±0.03	2.1±0.2	162±28	258±7	2.6±0.1	210±23	584±8
0.45±0.03	2.1±0.2	192±32	277±9	2.2±0.1	170±18	623±7
0.50±0.03	2.0±0.1	177±29	280±8	2.2±0.1	163±19	637±7
0.55±0.03	2.1±0.2	241±62	282±12	2.1±0.2	183±29	645±10
0.60±0.03	1.5±0.2	128±35	355±10	2.0±0.2	182±30	668±11
0.65±0.03	1.8±0.1	152±28	356±8	1.9±0.1	151±23	677±8
0.70±0.03	1.4±0.2	125±32	377±10	1.7±0.1	139±27	696±8
0.76±0.03	1.7±0.1	197±45	391±19	1.6±0.1	117±25	726±6
0.80±0.03	1.4±0.1	148±26	426±11	1.7±0.1	144±27	737±7
0.85±0.03	1.3±0.1	104±22	438±7	1.5±0.1	158±30	764±10
0.90±0.03	1.3±0.1	165±39	448±12	1.4±0.1	100±20	790±6
0.95±0.04	1.1±0.1	115±43	485±12	1.2±0.1	101±28	801±8
1.01±0.03	1.0±0.1	135±34	535±20	1.1±0.1	131±33	828±11
1.05±0.03	0.6±0.1	45 ±20	608±6	1.0±0.1	126±31	840±12
1.10±0.03	0.5±0.1	45 ±27	627^{+25}_{-13}	0.9±0.1	150^{+62}_{-42}	866±23
1.18±0.02	<0.7	75[b]	....	<0.9	75[b]	....
1.22±0.02	<0.8	75[b]	....	<0.8	75[b]	....

[a] The error on S_z is the standard deviation of the distribution of S_z values in the selection bin [b] Parameter fixed at this value

Lorentzian components which have centroid frequencies of 0.5 and 1.5 times that of the HBO.

The same function we used for our analysis of GX 5–1 was used in the analysis of the similar Z source GX 340+0 (Jonker et al. 2000b). There no third harmonic of the sub–HBO was found. Instead we found excess power (a shoulder)

close to the HBO peak, which when fit with a Lorentzian was at a frequency entirely inconsistent with 1.5 times that of the HBO. Reanalysis of those data with the insights gained by our work on GX 5–1 did not alter this conclusion. In GX 340+0 both the HBO and the NBO peak became asymmetric when they were strongest. Similar behaviour was

Table 5. Fit parameters of different functions describing the peak separation as a function of S_z. The broken functions are two straight lines concatenated at the break. The last row contains the χ^2 and the degrees of freedom (d.o.f.) of the fit. Note that unlike in the *top panel* of Fig 9 only independent measurements have been used in the *lower panel*.

	Constant	Linear	Parabola	Broken	Broken
Zeropoint	325±10 Hz	369±21 Hz	291 ± 29 Hz	334±4 Hz	348±9 Hz
Slope	....	−70 ± 30	259 ± 109	0^a	-24±15
Quadratic / break	....	....	−275 ± 90	$S_z = 0.93\pm0.06$	$S_z = 0.94\pm0.05$
Slope after Break	....	....	....	-832±483	-832±439
χ^2/d.o.f.	66.8 /9	39.9/8	15.0 / 7	7.8 / 7	5.5 / 6

[a] Parameter fixed at this value
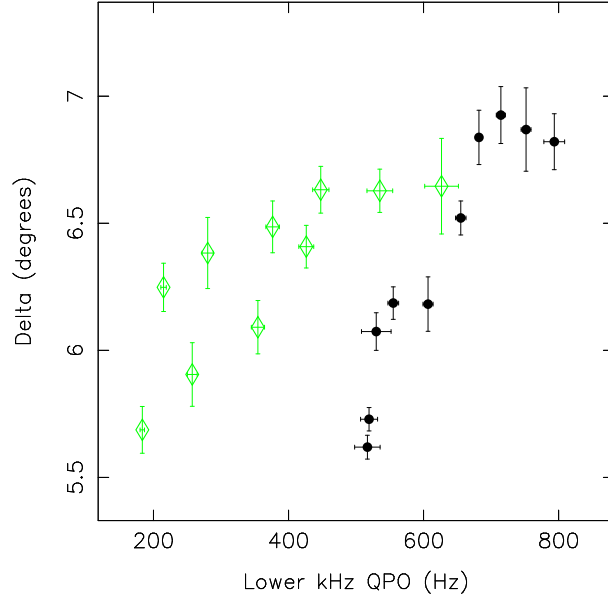
Figure 11. The angle δ (defined by Osherovich & Titarchuk 1999) for GX 5–1 (grey diamonds) and GX 17+2 (black dots) as a function of the lower kHz QPO frequency.

found in GX 5–1, where for $S_z < 0.5$ four of the five HBO measurements were done using two Lorentzians with centroid frequencies up to 2 Hz apart with similar FWHMs but different strengths, indicating that the HBO was asymmetric. However, unlike in our analysis of GX 340+0 where the data were selected according to HBO frequency, in the case of GX 5–1 this asymmetry could be an artifact of the selection method as explained in Section 3.2. An attempt to fit the average power spectra of GX 17+2 (Homan et al. 2001a) with the same fit function as that of GX 5–1 did not lead to the detection of a third harmonic to the sub–HBO. The asymmetry of the HBO found in GX 340+0 and the third harmonic of the sub–HBO found in GX 5–1 could be two different components, one of which is detected in each source because of the special circumstances affecting detections in each case: the larger amplitude of the HBO in GX 340+0 than in GX 5–1 allows to detect a strong asymmetric (shoulder) component, whereas the higher signal–to–noise in GX 5–1 than in GX 340+0 (due to the fact that GX 5–1 is several times brighter than GX 340+0) leads to the detection of the broad third harmonic. New observations with higher signal–to–noise ratios can reveal whether both components are present in both sources or whether they represent power provided by one single component.

The low–frequency power spectra of the three Z sources discussed above (GX 17+2, GX 340+0, GX 5–1) are quantitatively different. In Sco X–1 and GX 17+2 a QPO is found when the source is on the Flaring Branch (the FBO; Hasinger, Priedhorsky & Middleditch 1989; Penninx et al. 1990). Such a QPO is absent in GX 340+0, GX 5–1, GX 349+2, and Cyg X–2. The new component we found in the power spectrum of GX 5–1 with frequencies similar to those of the FBO when the source is on the Flaring Branch is much broader than the FBO in Sco X–1 and GX 17+2. The second harmonic of the HBO is relatively strong in GX 17+2 while for GX 5–1 and GX 340+0 only weak harmonics have been detected (see Hasinger & van der Klis 1989; van der Klis 1989). Furthermore, the fractional rms amplitude of the HBO is highest in GX 340+0, and lowest for GX 17+2. The HBO frequency in GX 17+2 was found to decrease on the Normal Branch (Wijnands et al. 1997a; Homan et al. 2001a), whereas in GX 340+0 and GX 5–1 the frequency is consistent with being constant (Jonker et al. 2000b). Besides the Lorentzians also the LFN properties are different; it is always peaked in GX 17+2 whereas this is never the case in GX 5–1 and GX 340+0 (see Hasinger & van der Klis 1989; van der Klis 1989; Homan et al. 2001a; Jonker et al. 2000b). The dependence of the HBO, lower and upper kHz QPO

Q–values on S_z is shown in Fig. 12. The HBO Q–value decreases gradually for $S_z > 0.5$, while that of the kHz QPOs increases. This is opposite to what was found for GX 17+2 (Homan et al. 2001a), where the Q–value of the HBO and that of the kHz QPOs increased as a function of S_z.

4.3   Comparing GX 5–1 with XTE J1550–564 and 4U 1608–52

In the power spectra of black hole candidates low–frequency QPOs with harmonics are occasionally found in the low, intermediate and very high state (e.g. GS 1124–68, Belloni et al. 1997b; GX 339–4, Méndez & van der Klis 1997; XTE J1550–564, Sobczak et al. 2000; Homan et al. 2001b). Occasionally, these black hole candidate QPOs have asymmetric profiles. We found a similar harmonic structure of QPOs in the Z source GX 5–1. The Q–values of the harmonics for XTE J1550–564 are similar to those found for GX 5–1: low Q–values for the odd harmonics and high Q–values for the even harmonics (Homan et al. 2001b). However, we checked the energy dependence of the QPOs in GX 5–1 and there are no indications of changes in the Q–values with energy as were found in XTE J1550–564 (Homan et al. 2001b). In general the energy dependence and time lag behaviour of the QPOs in GX 5–1 (Vaughan et al. 1999) is different from what was found in XTE J1550–564 (Wijnands, Homan & van der Klis 1999). On the Flaring Branch, similar to the High State in black hole candidates, the fractional rms amplitude of the variability is low, and QPOs are weak or absent (in GX 17+2 and Sco X–1, just as in XTE J1550–564 a QPO with a centroid frequency of ∼18 Hz is found, but whether they are related is unclear). The similarities between the Horizontal Branch variability and that of the Intermediate/Low State have been pointed out before (van der Klis 1994a; van der Klis 1994b; Wijnands & van der Klis 1999). Furthermore, the trend of a decrease in variability timescale as the source approaches the Flaring Branch/High State is the same in black hole candidates as in GX 5–1 and 4U 1608–52 (cf. Homan et al. 2001b; Méndez, van der Klis & van Paradijs 1998).

To further investigate the similarities between a black hole candidate (XTE J1550–564), a Z source (GX 5–1), and an atoll source (4U 1608–52) we created colour–colour diagrams (CDs) for the three sources in two ways. First, we used the colour definitions commonly used for atoll and Z sources (soft and hard colour were defined as the logarithm of the 3.6–6.2 / 2.5–3.6 keV and 9.8–16.0 / 6.2–9.8 keV count rate ratio, respectively). These CDs are shown in the *left panels* of Fig. 13, 14, and 15. Second, we created CDs in a similar way as van Teeseling & Verbunt (1994), an approach often used for black hole candidates (Belloni et al. 1997a; Homan et al. 2001b; although see also Miyamoto et al. 1991). We defined the hard and soft colour as the 9.7–16.0/ 2–6.4 keV and 6.4–9.7/ 2–6.4 keV count rate ratio for observations 1–41, respectively and that of the 9.7–15.8 / 2–6.6 keV and 6.6–9.7 / 2–6.6 keV count rate ratio for observations 42–76, respectively (Fig. 13, *right panel*). In case of the *right panels* for Fig. 14 and 15 the hard and soft colour were defined as the 16.0–19.4 / 2.2–6.2 keV, and 6.5–15.7 / 2.2–6.2 keV count rate ratio, respectively. Note that in the *right panels* the soft colour is plotted vs. the hard colour, as the convention, introduced by (Ostriker 1977) to plot hard colour vs.

soft colour was abandoned in some of the recent black hole work. In the *right panels* the points have been connected by a line. Lines bridging different parts of the diagrams do not reflect sudden jumps or changes in source state, but are due to gaps introduced by observational windowing.

A similar structure as for XTE J1550–564 was found in the CD of GX 5–1 (Figure 13, 14 *right panel*). The Flaring Branch is now vertical and located at the left side of the figure, similar to the High State in XTE J1550–564. The Normal Branch connects to the Flaring Branch and points towards the upper right corner of the diagram (both the hard colour and the soft colour increase as the source moves up the Normal Branch). The Horizontal Branch is a continuation of the Normal Branch, with only a slight bend at the Normal Branch–Horizontal Branch junction. (It is interesting to note that there is also no vertex present in GX 17+2 at the Horizontal– Normal Branch junction at energies above 14.8 keV, Figure 3C of Homan et al. 2001a). The 'Dipping' Flaring Branch is parallel to the Normal Branch but directed towards the lower left corner. The 'Dipping' Flaring Branch has been found in the Z sources Cyg X–2, GX 5–1 and GX 340+0 (Kuulkers, van der Klis & Vaughan 1996; Kuulkers et al. 1994; Jonker et al. 2000b). The CD of the atoll source 4U 1608–52 again shows a similar structure as found for XTE J1550–564 (Fig. 14, 15 *right panels*). The island state is found in the top right corner of the *right panel* of Fig. 15, whereas the lower banana branch connects to the upper banana branch in the lower left corner. The upper banana branch seems similar to the black hole candidate High State and the Z source Flaring Branch.

The CD of the black hole candidate XTE J1550–564, plotted using colours typically applied for neutron star sources is reminiscent of that of an atoll source, although more structure is observed (Fig. 14 *left panel*). The source was first found in the upper right part of the CD as the outburst started. The path traced by the source as the outburst progressed is indicated with arrows. For a complete description of the outburst of XTE J1550–564 we refer to Cui et al. (1999), Sobczak et al. (2000), and Homan et al. (2001b).

The similarities between the colour–colour diagrams of the Z source GX 5–1, the atoll source 4U 1608–52, and the black hole candidate XTE J1550–564 strengthen the idea that some of the spectral properties of LMXBs originate in the accretion disc and do not depend on the presence of a solid surface. However, our analysis also indicates that differences between spectral properties of the neutron star Z and atoll sources and the black hole candidates do exist (e.g., the *left panel* of Fig. 13, 14, and 15) but may not clearly show up in representations of the CD commonly used for black–hole candidates. The explanation for this could be that in the "black–hole colour scheme" only three independent colours are defined whereas in the "neutron star colour scheme" four colours are usually defined.

So, although the CDs of a Z or atoll source and that of a black hole candidate appear similar in shape when plotted using colours typical for black hole studies, their appearance is both dissimilar and more complicated when plotted using colours typical for neutron star studies. Whether the complications can be ascribed to the unique nature of the sources considered can only be checked by comparing more sources but the conclusion that dissimilar CDs can appear more similar than they really are in the "black hole" repre-
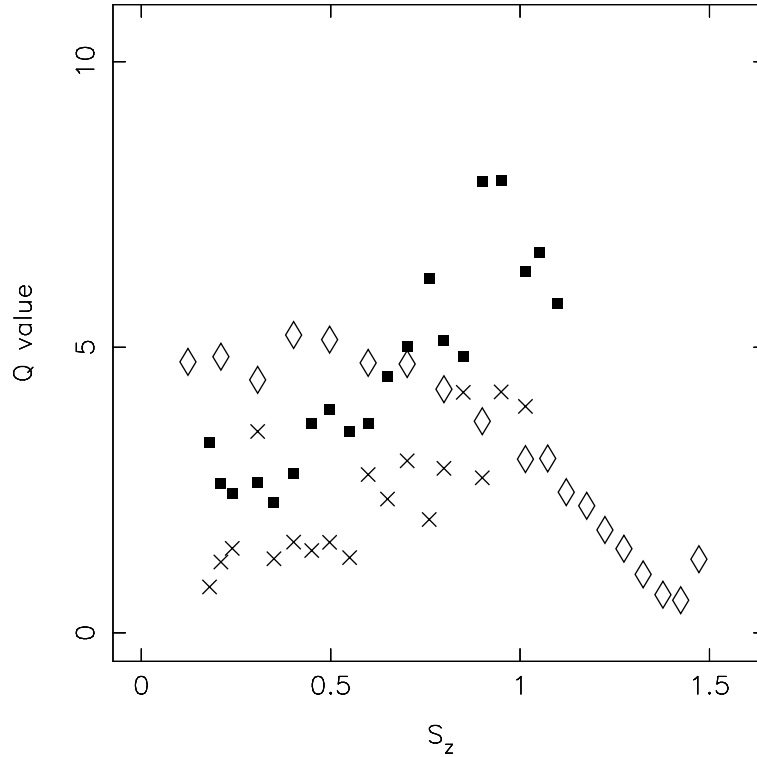
Figure 12. The Q–values of the HBO (diamonds), the lower (crosses), and the upper kHz QPO (filled squares) as a function of S_z. The Q–values of both kHz QPOs increase with increasing S_z, while that of the HBO decreases for $S_z > 0.5$. Error bars have been omitted for clarity. The errors of the diamonds (HBO) are ~ 1.5 times the size of the symbols. The errors of the crosses and squares (lower and upper kHz QPO, respectively) are of the order of the amplitude of the scatter in measurements close together in S_z.

sentation can already be drawn. Conclusions regarding the spectral state or properties of the source based on the colours commonly used in black hole candidates should be regarded with caution since an other choice of colours may lead to a qualitatively different CD.

REFERENCES

Alpar M. A., Shaham J., 1985, Nat, 316, 239

Belloni T., Mendez M., King A. R., van der Klis M., van Paradijs J., 1997, ApJ, 488, L109

Belloni T., van der Klis M., Lewin W. H. G., van Paradijs J., Dotani T., Mitsuda K., Miyamoto S., 1997, A&A, 322, 857

Bevington P. R., Robinson D. K., 1992, Data reduction and error analysis for the physical sciences. New York: McGraw-Hill, —c1992, 2nd ed.

Bradt H. V., Rothschild R. E., Swank J. H., 1993, A&AS, 97, 355

Braes L., Miley G., Schoenmakers A., 1972, Nat

Cui W., Zhang S. N., Chen W., Morgan E. H., 1999, ApJ, 512, L43

Di Salvo T. et al., 2000, ApJ, 544, L119

Di Salvo T., Méndez M., van der Klis M., Ford E., Robba N. R., 2001, ApJ, 546, 1107

Dieters S. W., van der Klis M., 2000, MNRAS, 311, 201

Ford E. C., van der Klis M., van Paradijs J., Méndez M., Wijnands R., Kaaret P., 1998, ApJ, 508, L155

Ford E. C., van der Klis M., Méndez M., Wijnands R., Homan J., Jonker P. G., van Paradijs J., 2000, ApJ, 537, 368

Hasinger G., van der Klis M., 1989, A&A, 225, 79

Hasinger G., Priedhorsky W. C., Middleditch J., 1989, ApJ, 337, 843

Hasinger G., van der Klis M., Ebisawa K., Dotani T., Mitsuda K., 1990, A&A, 235, 131

Hertz P., Vaughan B., Wood K. S., Norris J. P., Mitsuda K., Michelson P. F., Dotani T., 1992, ApJ, 396, 201

Homan J., van der Klis M., Jonker P. G., Wijnands R., Kuulkers E., Mendez M., Lewin W. G., 2001a, ApJ

Homan J., Wijnands R., van der Klis M., Belloni T., van Paradijs J., Klein-Wolt M., Fender R., Méndez M., 2001, ApJS, 132, 377

Jahoda K., Swank J. H., Giles A. B., Stark M. J., Strohmayer T., Zhang W., Morgan E. H., 1996, Proc. SPIE, 2808, 59

Jonker P. G., Fender R. P., Hambly N. C., van der Klis M., 2000, MNRAS, 315, L57
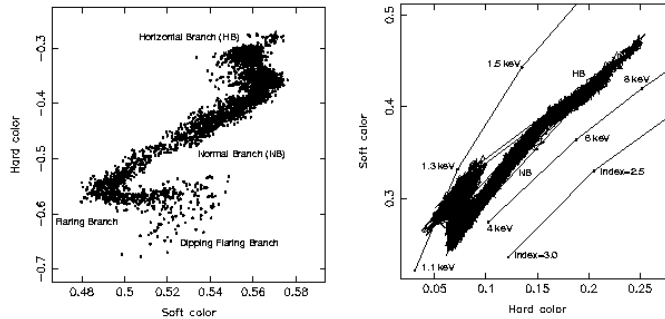
Figure 13. *Left panel:* Colour–colour diagram of observations 19–41 where the soft and hard colour were defined as the logarithm of the 3.6–6.2 / 2.5–3.6 keV and 9.8–16.0 / 6.2–9.8 keV count rate ratio, respectively. Each dot is a 64 s average. *Right panel:* Colour–colour diagram of the 6.4–9.7 / 2–6.4 keV (or 6.6–9.7 / 2–6.6 keV for observations 42–76; soft colour) count rate ratio vs. the 9.8–16.0 / 2–6.4 keV (or 9.7–15.8 / 2–6.6 keV for observations 42–76; hard colour). Each 512 s average is connected to the next by a line. The lines in the *right panel* indicate what RXTE would have seen if the source spectrum had consisted of only a blackbody (top), a thermal bremsstrahlung (middle), or a powerlaw (bottom line) spectrum. In this Figure as well as in Figure 14, and 15 error bars were omitted for clarity; data were background subtracted but no deadtime corrections were applied (the deadtime was in all cases less than 4%).

Jonker P. G. et al., 2000, ApJ, 537, 374

Jonker P. G. et al., 2001, ApJ

Kaaret P., Ford E. C., Chen K., 1997, ApJ, 480, L27

Kluzniak W., 1993, A&AS, 97, 265

Kuulkers E., van der Klis M., Oosterbroek T., Asai K., Dotani T., van Paradijs J., Lewin W. H. G., 1994, A&A, 289, 795

Kuulkers E., van der Klis M., Vaughan B. A., 1996, A&A, 311, 197

Lamb F. K., Shibazaki N., Alpar M. A., Shaham J., 1985, Nat, 317, 681

Lewin W. H. G., Lubin L. M., Tan J., van der Klis M., van Paradijs J., Penninx W., Dotani T., Mitsuda K., 1992, MNRAS, 256, 545

Markwardt C. B., Strohmayer T. E., Swank J. H., 1999, ApJ, 512, 125

Méndez M., van der Klis M., 1997, ApJ, 479, 926

Méndez M., van der Klis M., 1999, ApJ, 517, L51

Méndez M., van der Klis M., Wijnands R., Ford E. C., van Paradijis J., Vaughan B. A., 1998, ApJ, 505, L23

Méndez M., van der Klis M., van Paradijs J., 1998, ApJ, 506, L117

Miller M. C., Lamb F. K., Psaltis D., 1998, ApJ, 508, 791

Miyamoto S., Kimura K., Kitamoto S., Dotani T., Ebisawa K., 1991, ApJ, 383, 784

Osherovich V., Titarchuk L., 1999, ApJ, 523, L73

Ostriker J. P., 1977, in Annals of the New York academy of sciences; Eighth Texas symposium on relativistic astrophysics. p. 229

Penninx W., Lewin W. H. G., Mitsuda K., van der Klis M., van Paradijs J., Zilstra A. A., 1990, MNRAS, 243, 114

Psaltis D., Norman C., 2001, ApJ, , submitted

Sobczak G. J., McClintock J. E., Remillard R. A., Cui W., Levine A. M., Morgan E. H., Orosz J. A., Bailyn C. D., 2000, ApJ, 544, 993

Stella L., Vietri M., 1998, ApJ, 492, L59

Stella L., Vietri M., 1999, Phys. Rev. Lett

Titarchuk L., Lapidus I., Muslimov A., 1998, ApJ, 499, 315+

van der Klis M., Jansen F., van Paradijs J., Lewin W. H. G., van den Heuvel E. P. J., Trumper J. E., Szatjno M., 1985, Nat, 316, 225

van der Klis M., Wijnands R. A. D., Horne K., Chen W., 1997, ApJ, 481, L97

van der Klis M., 1989, ARA&A, 27, 517

van der Klis M., 1994, A&A, 283, 469

van der Klis M., 1994, ApJS, 92, 511

van der Klis M., 1995, in Proceedings of the NATO Advanced Study Institute on the Lives of the Neutron Stars, held in Kemer, Turkey, August 29-September 12, 1993. Editors, M.A. Alpar, U. Kiziloglu, and J. van Paradijs; Publisher, Kluwer Academic, Dordrecht, The Netherlands, Boston, Massachusetts. p. p. 301

van der Klis M., 1998, in NATO ASIC Proc. 515: The Many Faces of Neutron Stars. p. 337

van der Klis M., 2000, ARA&A, 38, 717

van Straaten S., Ford E. C., van der Klis M., Méndez M., Kaaret P., 2000, ApJ, 540, 1049

van Teeseling A., Verbunt F., 1994, A&A, 292, 519

Vaughan B. A., van der Klis M., Lewin W. H. G., van Paradijs J., Mitsuda K., Dotani T., 1999, A&A, 343, 197

Vrtilek S. D., Penninx W., Raymond J. C., Verbunt F., Hertz P., Wood K., Lewin W. H. G., Mitsuda K., 1991, ApJ, 376, 278

Wijnands R., van der Klis M., 1999, ApJ, 514, 939

Wijnands R., Homan J., van der Klis M., 1999, ApJ, 526, 33
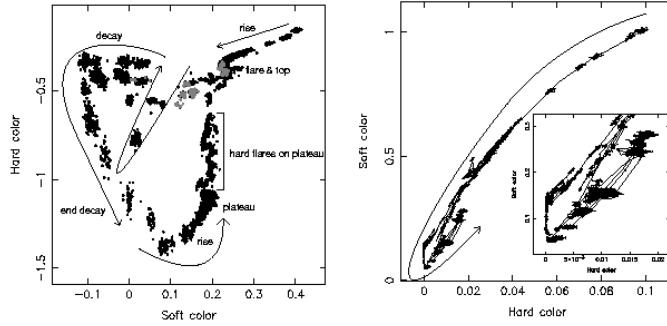
Figure 14. *Left panel:* Colour–colour diagram of XTE J1550–564. We used all data obtained with the RXTE satellite of XTE J1550–564 during the interval MJD 51065–51259 (gain epoch 3); soft and hard colours were defined as in Fig. 13 (*left panel*). Each dot is a 64 s average. The path the source traces as the outburst progresses is indicated. The grey dots are the last days of observations just before the gain change. *Right panel:* Colour–colour diagram of the same data as in the *left panel*. Note that the soft colour is plotted vs. hard colour. The hard and soft colour were defined as the 16.0–19.4 / 2.2–6.2 keV, and 6.5–15.7 / 2.2–6.2 keV count rate ratio, respectively. Each 64 s average is connected to the next by a line. A zoom–in of the lower left corner is visible to the right. The arrow indicates the source changes as the outburst progressed.
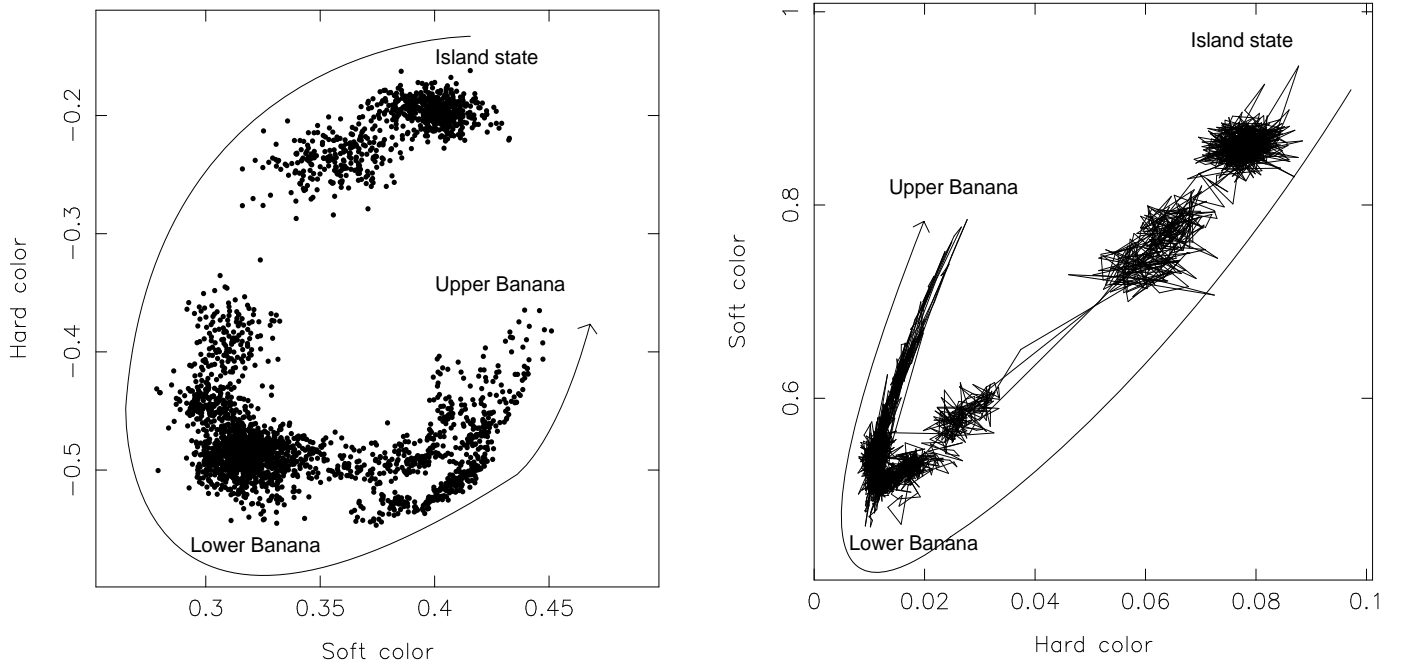
Figure 15. *Left panel:* Colour–colour diagram of 4U 1608–52. We used the same data as was used by Méndez et al. (1998). Soft and hard colours where defined as in Fig. 13 (*left panel*). Each dot is a 64 s average. *Right panel:* Colour–colour diagram of the same data as in the *left panel*. Note that the soft colour is plotted vs. hard colour. The hard and soft colour were defined as in Fig. 14. Each 64 s average is connected to the next by a line. The arrow indicates the direction of increase in inferred mass accrettion rate.

Wijnands R. A. D., van der Klis M., Psaltis D., Lamb F. K.,
    Kuulkers E., Dieters S., van Paradijs J., Lewin W. H. G.,
    1996, ApJ, 469, L5
Wijnands R. et al., 1997, ApJ, 490, L157
Wijnands R. A. D., van der Klis M., Kuulkers E., Asai K.,
    Hasinger G., 1997, A&A, 323, 399
Wijnands R., Mendez M., van der Klis M., Psaltis D.,
    Kuulkers E., Lamb F. K., 1998, ApJ, 504, L35
Zhang W., Smale A. P., Strohmayer T. E., Swank J. H., 1998,
    ApJ, 500, L171
Zhang W., Strohmayer T. E., Swank J. H., 1997, ApJ, 482, L167